




Peripheral chiral spin textures and topological Hall effect in CoSi nanomagnets

Rabindra Pahari ^{1,2,*} Balamurugan Balasubramanian,^{1,2} Ahsan Ullah,^{1,2} Priyanka Manchanda,³ Hiroaki Komuro ^{1,4}
 Robert Streubel,^{1,2} Christoph Klewe,⁵ Shah R. Valloppilly,¹ Padraic Shafer,⁵ Pratibha Dev ³
 Ralph Skomski,^{1,2} and David J. Sellmyer^{1,2,†}

¹Nebraska Center for Materials and Nanoscience, University of Nebraska, Lincoln, Nebraska 68588, USA

²Department of Physics and Astronomy, University of Nebraska, Lincoln, Nebraska 68588, USA

³Department of Physics and Astronomy, Howard University, Washington, DC, 20059, USA

⁴Department of Cardiovascular Medicine, Tokyo Medical and Dental University, Tokyo 113-8510, Japan

⁵Advanced Light Source, Lawrence Berkeley National Laboratory, Berkeley, California 94720, USA



(Received 14 April 2021; accepted 10 December 2021; published 29 December 2021)

The spin structure and transport behavior of B20-ordered CoSi nanomagnets are investigated experimentally and by theoretical calculations. B20 materials are of interest in spin electronics because their noncentrosymmetric crystal structure favors noncoplanar spin structures that yield a contribution to the Hall effect. However, stoichiometric bulk CoSi is nonmagnetic, and combining magnetic order at and above room temperature with small feature sizes has remained a general challenge. Our CoSi nanoclusters have an average size of 11.6 nm and a magnetic ordering temperature of 330 K. First-principle calculations and x-ray circular dichroism experiments show that the magnetic moment is predominantly confined to the shells of the clusters. The CoSi nanocluster ensemble exhibits a topological Hall effect, which is explained by an analytical model and by micromagnetic simulations on the basis of competing Dzyaloshinskii-Moriya and intra- and intercluster exchange interactions. The topological Hall effect is caused by formation of chiral spin textures in the shells of the clusters, which exhibit fractional skyrmion number and are therefore termed as paraskyrmions (closely related to skyrmion spin structures). This research shows how nanostructuring of a chiral atomic structure can create a spin-textured material with a topological Hall effect and a magnetic ordering temperature above room temperature.

DOI: [10.1103/PhysRevMaterials.5.124418](https://doi.org/10.1103/PhysRevMaterials.5.124418)

I. INTRODUCTION

The understanding and control of topological and emergent properties of matter through nanoscale structuring is a topic of great current interest in both science and technology, especially in spin electronics [1–4]. It is well known that noncoplanar spin structures in conducting magnets give rise to a Hall-effect contribution known as the topological Hall effect (THE) [5,6], thin-film skyrmions being the prime example [5–8]. Miniaturization requires small-scale magnetic feature sizes [9–11] at and above room temperature, which is difficult to achieve due to the competition between Dzyaloshinskii-Moriya (DM) interaction (D) and interatomic exchange \mathcal{J} . Increasing the former reduces the feature or skyrmion size $\lambda \sim \mathcal{J}/D$ [12–20], whereas the latter has the opposite effect of being adverse to miniaturization. The exchange can be reduced by using a material having a low Curie temperature $T_c \sim \mathcal{J}/k_B$, but this approach is contradictory to the aim of having a THE at and above room temperature. Examples are FeGe ($T_c = 278$ K), which exhibits a relatively large skyrmion size ($\lambda = 70$ nm) compared to MnSi ($T_c = 30$ K and $\lambda = 18$ nm) [12], as well as inverse tetragonal Heusler

compounds and multilayered thin-film systems with feature sizes generally larger than 100 nm [4,21–23].

The THE is caused by conduction electrons exchange-interacting with neighboring atomic moments \mathbf{M}_i that are not only noncollinear but also noncoplanar, Fig. 1(a). The corresponding spin rotation creates a Berry curvature [24] that translates into an emergent magnetic field B_{eff} [green arrow in Fig. 1(a)] and yields the THE. The emergent magnetic field is proportional to the triple product $\chi_{\text{TP}} = \mathbf{M}_1 \cdot (\mathbf{M}_2 \times \mathbf{M}_3)$, whose continuum equivalent is $\Phi = \mathbf{M} \cdot (\partial \mathbf{M} / \partial x \times \partial \mathbf{M} / \partial y) / 4\pi$. Several names have been given to these entities, but there is some ambiguity. The quantity χ_{TP} is often referred to as scalar spin chirality, but true chirality implies, by definition, a distinction between left- and right-handedness [25]. Some systems, such as multilayers with C_{nv} symmetry, are neither structurally nor magnetically chiral but have a nonzero χ_{TP} . The quantity Φ is known as the *skyrmion density* [8,26], but it is important to keep in mind that Φ is generally different from the number of skyrmions per unit area. The THE is obtained by areal integration $Q = \int \Phi dx dy$, and this integral is quantized ($Q = \pm 1$) for skyrmions but not for other skyrmionic spin structures [27] that may be termed partial skyrmions or “paraskyrmions.” The equation for Φ means that the THE is a functional of the local magnetization $\mathbf{M}(\mathbf{r})$, that is, the THE is determined by the local magnetization and its gradient, which is strongly influenced by the exchange and DM interactions. A key question is therefore to relate the THE to the nanoscale spin structure $\mathbf{M}(\mathbf{r})$.

*Present address: Department of Electrical and Computer Engineering, University of Minnesota, Minneapolis, MN 55455, USA.

†Corresponding author: dsellmyer@unl.edu

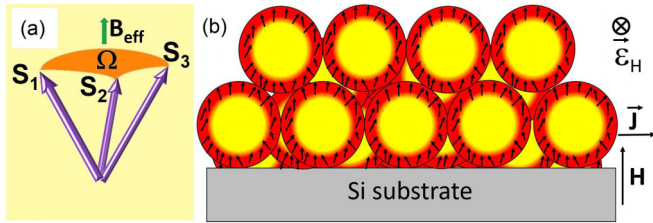


FIG. 1. Spin structure of CoSi: (a) triple-product spin configuration yielding a THE contribution, (b) schematic nanoscale geometry and spin structure, where \mathbf{H} , \mathbf{J} , and ϵ correspond to applied magnetic field, current density, and Hall emf, respectively.

B20 compounds such as $T_{50}X_{50}$ ($T = \text{Fe, Co, Mn}$ and $X = \text{Ge, Si}$) are promising spintronics materials, because their noncentrosymmetric and chiral crystal structure leads to scalar DM interactions, which create spin spirals with well-defined helicity in the bulk [12–20] and skyrmions in homogeneous thin films. We have recently used nanostructuring to achieve room-temperature skyrmions with sizes of about 17 nm through exchange engineering in a B20-type bulk $\text{Co}_{1.043}\text{Si}_{0.957}$ [28]. However, this exchange engineering involves nonstoichiometric crystals and a quantum phase transition because equiatomic CoSi is nonmagnetic. In this article, we show that nanostructuring can be used to resolve the size-vs-temperature dilemma on a length scale of about 10 nm or less, exploiting that the scalar DM interaction in B20 magnets enhances Φ . Our previous studies have shown that an inert-gas plasma-condensation-type cluster-deposition method is promising in fabricating other CoSi compounds such as Co_3Si and Co_2Si , which form noncubic centrosymmetric crystal structures and show controllable ferromagnetic properties upon nanostructuring [29,30].

II. METHODS AND RESULTS

Our thin films consist of B20-ordered CoSi nanoclusters having an average size of 11.6 nm. Figure 1(b) summarizes schematically the structural and measurement geometry of the nanocluster film. The cluster-deposition method was used to produce CoSi nanoclusters and deposit them onto room-temperature substrates for an extended time to form dense films of thickness about 200 nm.

The projector-augmented-wave method (PAW), as implemented in the Vienna *ab-initio* simulation package (VASP), was employed to carry out the first-principles calculations [31,32]. Micromagnetic simulations were carried out using MuMax3 to determine the spin structures in CoSi nanoclusters [33]. More details on the experimental and computational methods are discussed in the Supplemental Materials S1–S3 [34].

A. Structure

Figure 2(a) shows a unit cell of the noncentrosymmetric cubic B20 structure (point group T , space group $P2_13$, and prototype FeSi). X-ray diffraction (XRD) patterns of CoSi nanoclusters and polycrystalline bulk CoSi [Fig. 2(b)] are indexed to the cubic B20 structure [35]. An additional XRD peak seen in the nanocluster sample corresponds to the (111)

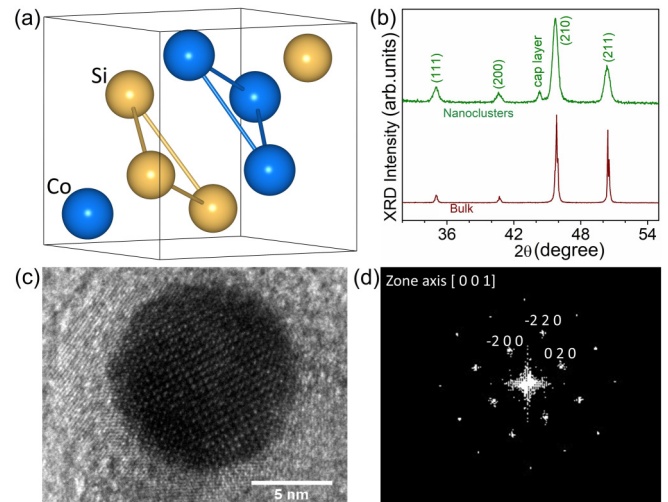


FIG. 2. Structure of CoSi: (a) unit cell, (b) x-ray diffraction pattern for bulk and nanoclusters, (c) HRTEM image of a nanocluster, and (d) the corresponding fast Fourier transform pattern indexed with the cubic B20 structure along the (001) zone axis.

reflection from the carbon cap layer [36]. A high-resolution transmission-electron microscopy (HRTEM) image of a CoSi nanocluster [Fig. 2(c)] and the fast Fourier transform (FFT) of the HRTEM image along the (001) zone axis [Fig. 2(d)] also confirm the B20 cubic structure.

In brief, XRD and HRTEM results show that the nanoclusters form the cubic B20 structure similar to polycrystalline bulk CoSi. The average grain sizes determined from x-ray diffraction data using Scherrer’s equation [37] are 34.8 nm (bulk) and 12.7 nm (nanoclusters). The latter value is a close agreement with the average cluster size of 11.6 nm determined from the TEM results (Supplemental Material S2).

B. Magnetism

Figures 3(a) and 3(b) show the field dependences of the low- and room-temperature magnetizations of bulk (a) and nanoclustered CoSi (b) measured using SQUID (superconducting quantum interference device) magnetometry. The bulk alloy does not order magnetically, and its susceptibility shows a crossover from positive (paramagnetic) at low temperatures to negative (diamagnetic) near 160 K, similar to the behavior observed in CoSi single crystals [38], whereas the nanoclusters have a high Curie temperature of about 330 K (see Supplemental Material S4).

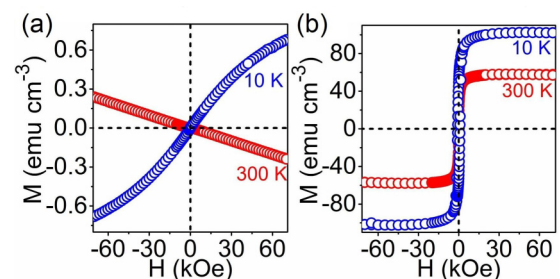


FIG. 3. Magnetization of CoSi: (a) bulk and (b) nanoclusters.

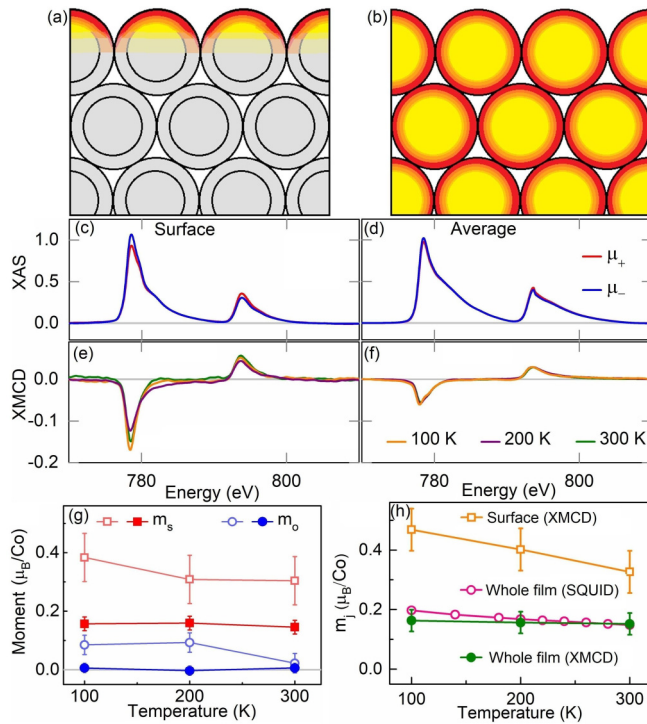


FIG. 4. Schematic structure and X-ray absorption spectra (XAS) for CoSi nanocluster film near Co $L_{3,2}$ edges ($2p \rightarrow 3d$): (a), (b) Schematic of the nanocluster film, where the red, orange, and yellow regions represent the strongly spin-polarized surface, spin-polarized intermediate region, and the almost nonmagnetic core, respectively. The top surface in (a) shows the region from which the surface XAS spectra originate. XAS and XMCD spectra of the surface and volume-average (whole film) regions [(c) and (e) and (d) and (f), respectively]. (g) Spin (m_s) and orbital (m_o) moments at different temperatures. The filled and empty symbols are moment contributions from the whole CoSi film thickness (average) and film surface, respectively. (h) Magnetic moments ($m_j = m_o + m_s$) obtained from XMCD and SQUID for the surface and whole CoSi film.

To experimentally investigate the magnetization distribution, we measured x-ray absorption spectroscopy (XAS) data near the Co $L_{3,2}$ edges (760–830 eV) for the CoSi nanocluster film in the presence of an external magnetic field (± 3 kOe) normal to the sample surface. The XAS spectra were retrieved from two parallel detection channels: (i) the current of electrons emanating from the surface of the CoSi nanocluster film and (ii) after passing completely through the nanocluster film. The former approach provides a probing depth of about 6 nm into the film, schematically shown as the colored region in Fig. 4(a), whereas the latter contains information about volume-averaged (average) properties from the whole CoSi film, as schematically shown in Fig. 4(b).

Figure 4(c) shows the XAS spectra for the photon angular momentum parallel (μ_+) and antiparallel (μ_-) to the applied magnetic field at 300 K from the surface (a) and from the whole film (b). The x-ray magnetic circular dichroism (XMCD) signal was obtained from the difference between the corresponding blue (μ_-) and red (μ_+) curves in Figs. 4(c) and 4(d) and is shown for different temperatures in Fig. 4(e) and Fig. 4(f), respectively. Orbital and spin moments (m_o and

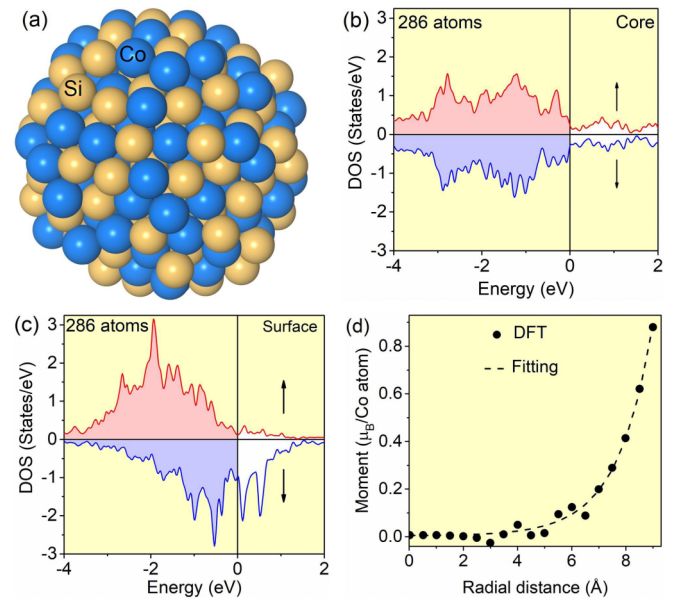


FIG. 5. DFT calculations on CoSi nanoclusters having 286 atoms. A schematic of the nanocluster (a). Average densities of states for surface Co atoms (b) and core Co atoms (c). Radial distribution of the magnetic moment per Co atom from the center of the cluster (solid circles) is fitted using a decay function, dashed line (d).

m_s , respectively) from the surface and whole film at different temperatures were obtained from the corresponding XAS and XMCD spectra [39,40] (see Supplemental Material S5 for more details) and are shown in Fig. 4(g). The magnetic moments, $m_j = m_o + m_s$, measured from the surface and whole film, are compared with the values measured using SQUID magnetometry in Fig. 4(h). The magnetization near the surface is higher than the magnetization of the whole film (see Supplemental Material S6 for more explanation).

To understand the nanocluster magnetism, we have performed density-functional-theory (DFT) calculations for the CoSi cluster shown in Fig. 5(a), which has 286 atoms (Supplemental Material S1). Figures 5(b) and 5(c) correspond to the average DOS calculated from the innermost core Co atoms (three Co atoms situated near the center of the cluster) and outermost 37 surface Co atoms, respectively. The calculated spin polarization, that is, the difference between the local \uparrow and \downarrow densities of states, is virtually zero in the cluster core, Fig. 5(b), whereas the nanocluster surface exhibits a large magnetic magnetization of $m' = 0.88 \mu_B$ per Co atom, Fig. 5(c). The calculated average magnetic moments for the core is $0.02 \mu_B/\text{Co}$. This indicates that the atoms near the surface spin-polarize the interior Co atoms.

Analytically, the radial dependence of the magnetization $m(r)$ for a spherical cluster with a radius R approximately obeys the preasymptotic differential equation $-\nabla^2 m + \kappa^2 m = 0$, whose solution is $m(r) = m' \frac{R \sinh(\kappa r)}{r \sinh(\kappa R)}$ [29]. Fitting the above equation to the DFT moments using $m' = 0.88 \mu_B/\text{Co}$ [Fig. 5(d)] yields an inverse decay length $\kappa = 0.88/\text{\AA}$, which suggests that the magnetic moments of Co atoms are mostly situated within a shell thickness of about 0.5 nm from the cluster surface. The average moment is $0.26 \mu_B/\text{Co}$ estimated

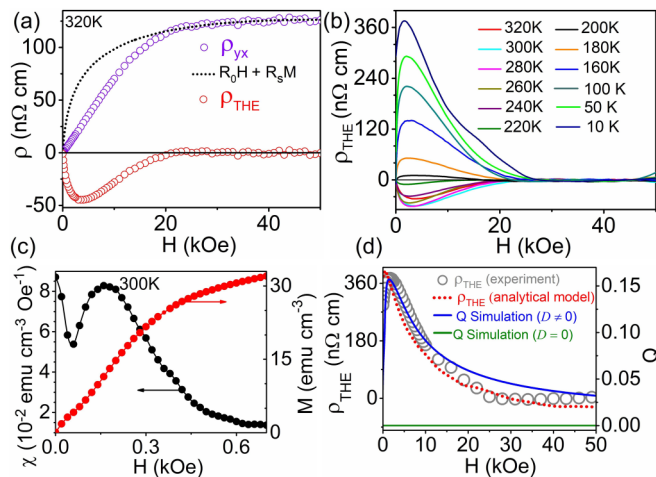


FIG. 6. Hall resistivity and dc susceptibility of the CoSi nanocluster film: (a) THE analysis at 320 K, (b) topological Hall resistivity as a function of field and temperature, (c) field dependences of magnetization M and dc susceptibility $\chi = dM/dH$ at 300 K, and (d) comparison of experimental and theoretical field dependences of the THE and skyrmion number (Q).

from moments of all Co atoms in the cluster, comparable to $0.24 \mu_B/\text{Co}$ at 10 K measured using SQUID.

C. Topological Hall effect

A widely used experimental method to determine the THE, also used as the starting point in the present paper, is to use the equation $\rho_{yx} = R_0H + R_sM + \rho_{\text{THE}}$ [8,26]. Here ρ_{yx} is the measured Hall resistivity, R_0H is the ordinary Hall effect, R_sM is the conventional [41] contribution to the anomalous Hall effect, and ρ_{THE} is the Berry-phase contribution to the anomalous Hall effect, or simply topological Hall effect. When the magnetization approaches saturation, R_sM_s becomes a constant, R_0 and R_s can be determined by plotting ρ_{yx}/H vs M/H in the high-field region (20–50 kOe), and $R_0H + R_sM$ can then be subtracted from ρ_{yx} to yield ρ_{THE} [27,42,43]. We have measured the Hall resistivity of the CoSi nanoclusters for temperatures below T_c and in magnetic fields of up to 50 kOe, applied perpendicular to the film plane. Figure 6(a) shows a typical Hall-effect analysis, namely, at 320 K, comparing total Hall effect (purple) with $R_0H + R_sM$ (black) and with the THE (red). The field and temperature dependence of the corresponding THE is shown in Fig. 6(b). The THE is often accompanied by anomalies in the magnetization $M(H)$ and in the dc susceptibility $\chi = dM/dH$, and Fig. 6(c) shows that such anomalies also exist in the present nanocluster thin films (see also Supplemental Material S8). The longitudinal resistivity of the CoSi nanocluster film at 10 K is about $50 \mu\Omega \text{ cm}$ (Fig. S7), an order of magnitude higher than bulk value, and this is due to the fact that the conduction proceeds through the contact points between the nanoclusters.

Figure 6(d) compares the experimental THE measured at 10 K (open circle) with theoretical calculations. The dotted red curve in Fig. 6(d) has been obtained by solving an analytical model yielding $\chi_{\text{TP}} = \mathbf{M}_1 \cdot (\mathbf{M}_2 \times \mathbf{M}_3)$. The calculation assumes three spins forming an angle θ with the film plane,

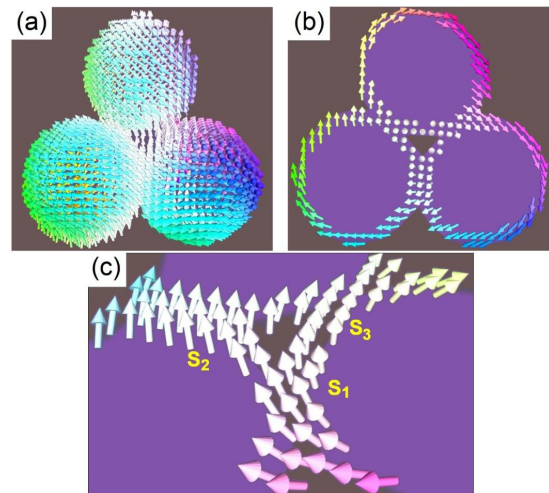


FIG. 7. Simulated spin structures in CoSi nanoclusters: (a) three-dimensional view on magnetic shell, (b) two-dimensional cross-section view on the equator plane, and (c) spin structure in the vicinity of the contact points (c). In this figure, the field was taken as 1.6 kOe, roughly corresponding to the THE maximum, and a nonzero D has been used (Supplemental Material S9), as appropriate for B20 materials. Note the poles of the spin structures in (a), which are distantly related to bobbars [45].

Fig. 1(a). The spins are subjected to an easy-plane uniaxial anisotropy of magnetostatic origin, which tries to keep the magnetizations in the film plane ($\theta = 90^\circ$). For such a configuration, the response to an external field is well known, namely, a straight line $M_z = M_s \cos\theta \sim H$. The evaluation of the corresponding triple product is straightforward and yields $\chi_{\text{TP}} = 3\sqrt{3}/2M_s^3 f(\theta)$, where $f(\theta) = \cos\theta \sin^2\theta$. In terms of the normalized magnetization $m = M_z/M_s$, we obtain $f(m) = m(1-m^2)$, which is the dotted red curve in Fig. 6(d).

III. DISCUSSION

While magnetization and susceptibility anomalies are an indication of THE, a proof requires analysis of $\mathbf{M}(\mathbf{r})$ and $\Phi(\mathbf{r})$. To obtain explicit information, we have used MuMax3 and carried out micromagnetic simulations using experimental parameters (see details in the Supplemental Material, S1 and S9). Figure 7 shows the spin structure obtained in our simulations. Without loss of generality, the figure is limited to three nanoclusters in contact with each other.

We have also investigated many-cluster systems, where the spin structure is very similar to Fig. 7 but difficult to visualize. The subfigures show the spin distribution in the magnetic shell (a), the corresponding equatorial cross-sectional view (b), and the spin structure in the vicinity of the contact points (c). The three spins S_1 , S_2 , and S_3 are clearly noncoplanar and forms chiral spin textures [similar to Fig. 1(a)], causing the conduction electrons to accumulate a Berry phase and to contribute to the Hall effect. The presence of B20-type scalar DM interactions (D) is essential for the formation of the noncoplanar spin structure in the present sample [blue curve in Fig. 6(d)]; by choosing $D = 0$, the simulations cause the THE to collapse [green line in Fig. 6(d)]. Note that the magnetocrystalline anisotropy of the CoSi clusters is small and does not affect

the spin structures according to our simulations. There is a probably also some C_{nv} -type surface DM interaction (Figs. 1 and 2 in Ref. [44]), which yields additional noncoplanarity but is ignored in the present simulations. Note that the addition of other DMI terms would somewhat modify the spin structures of Fig. 7 but does not change the overall picture, namely, the creation of the Berry phase and corresponding THE.

The total THE contribution corresponds to $Q \approx 0.15$ per nanocluster, as estimated by numerical integration over Φ . Along the surface and through the contact points, the feature or “paraskyrmion” size, deduced from the magnetization gradient in Φ , is of the order of 10 nm. Figure 7(c) visualizes the filigree nature of the CoSi paraskyrmions. Note that both intra- and intercluster exchange interactions are involved in the nanoscale confinement of $\mathbf{M}(\mathbf{r})$ and $\Phi(\mathbf{r})$.

Our above-outlined experimental and theoretical findings prove the existence of paraskyrmions in CoSi nanocluster films. While the spin structure of Fig. 7 unambiguously yields THE signatures such as those in Fig. 6, there may be other contributions. One mechanism is thermal spin-chirality fluctuations, which exist, for example, in thin films with perpendicular magnetic anisotropy. The chiral spin fluctuations may cause or contribute to sign changes in the Hall effect [46–48], a feature we also see in our data THE above 210 K, Fig. 6(b). In terms of Fig. 7(c), these fluctuations would correspond to a thermally activated noncoplanarity of the spins. However, they are limited to the vicinity of T_c [46–49], while our CoSi nanocluster film exhibits a THE down to 10 K, far below T_c . Note that the chiral spin fluctuations may also cause or contribute to the observed sign change of the Hall effect [46,48], but this interpretation is not conclusive and somewhat speculative, and thermally fluctuating magnetic moments cannot explain the low-temperature effect that we observe even after considering the relatively small number of spins. In addition, the nanocluster film also exhibits a metal to semiconductor like transition in the longitudinal resistivity data (Supplemental Material S7). Therefore a comprehensive explanation of the temperature dependence of the Hall transport in core-shell structures close to the Stoner transition (and generally in B20 magnets) is a major challenge to future research.

From the viewpoint of first-principles theory, bulk CoSi is a semimetal close to a transition between diamagnetism and Pauli paramagnetism. It has a complicated Weyl-point structure near the Fermi level, which could give rise to a Hall-effect contribution, Eqs. (2) and (6) in Ref. [41]. However, the bulk CoSi in the core is nonmagnetic, whereas the magnetic CoSi in the surface shell has a very different electronic structure, Fig. 5, so the intrinsic contribution to the Hall effect is virtually zero.

A third mechanism is Hall-effect anomalies that may arise from multichannel Hall effects. The equation $\rho_{yx} = R_0 H + R_s M + \rho_{\text{THE}}$ is limited to *homogeneous (single-phase)* thin films and cannot be easily generalized to inhomogeneous

thin films [50,51]. The reason is that the current density (responsible for skyrmionic spin density and THE) and the magnetization are generally realized in different spatial locations. The corresponding corrections are large in some systems, for example, in hard-soft composites having a bimodal switching-field distribution [51]. In our CoSi thin-film structures, the THE is largely given by currents traversing the sample, that is, going through the contact points. The surface spins away from the contact points fully contribute to the magnetization but only partially to the Hall resistivity. The THE contribution from the contact points is not suppressed by this mechanism, because our system is rather soft, with a very narrow switching-field distribution, and most of the sample inhomogeneity is associated with regions that contribute virtually nothing to M and to ρ_{THE} (core of the CoSi nanomagnets and vacuum).

IV. CONCLUSIONS

In summary, we found a substantial topological Hall effect in ensembles of CoSi nanoclusters. In contrast to bulk CoSi, which is nonmagnetic, the nanoclusters are magnetically ordered at room temperature. The magnetization is confined to a thin surface shell and forms peripheral chiral spin textures that we call paraskyrmions. The small feature size of about 10 nm or less is effected by B20-type Dzyaloshinskii-Moriya interactions in CoSi and may lead to new room-temperature spin-electronics approaches. See Supplemental Material for additional details on methods and results [34], which also includes Refs. [52–63].

ACKNOWLEDGMENTS

This research is primarily supported by NSF-DMREF: SusChEM under Grant No. 1729288 (fabrication and characterization). We acknowledge support from the U.S. Department of Energy under Award No. DE-FG02-04ER46152 (DFT calculations), the National Science Foundation/EPSCoR RII Track-1: Emergent Quantum Materials and Technologies (EQUATE) under Grant No. OIA-2044049 and NU Collaborative Initiative (Micromagnetic simulations), and Nebraska EPSCoR FIRST under Grant No. OIA-1557417 (XAS and XMCD characterization and analysis). This work was performed in part in the Nebraska Nanoscale Facility and Nebraska Center for Materials and Nanoscience, which are supported by the National Science Foundation under Award No. ECCS: 2025298, and the Nebraska Research Initiative. This research used resources of the Advanced Light Source, which is a DOE Office of Science User Facility under Contract No. DE-AC02-05CH11231 and the Holland Computing Center of the University of Nebraska for performing micromagnetic simulations.

[1] E. Skoropata, J. Nichols, J. M. Ok, R. V. Chopdekar, E. S. Choi, A. Rastogi, C. Sohn, X. Gao, S. Yoon, T. Farmer, R. D.

Desautels, Y. Choi, D. Haskel, J. W. Freeland, S. Okamoto, M. Brahlek, and H. N. Lee, *Sci. Adv.* **6**, eaaz3902 (2020).

- [2] M. V. Sapozhnikov, N. S. Gusev, S. A. Gusev, D. A. Tatarskiy, Yu. V. Petrov, A. G. Temiryazev, and A. A. Fraerman, *Phys. Rev. B* **103**, 054429 (2021).
- [3] A. Soumyanarayanan, M. Raju, A. L. G. Oyarce, A. K. C. Tan, M. Y. Im, A. P. Petrovic, P. Ho, K. H. Khoo, M. Tran, C. K. Gan, F. Ernult, and C. Panagopoulos, *Nat. Mater.* **16**, 898 (2017).
- [4] A. Fert, N. Reyren, and V. Cros, *Nat. Rev. Mater.* **2**, 17031 (2017).
- [5] C. Pfleiderer and A. Rosch, *Nature (London)* **465**, 880 (2010).
- [6] C. S. Spencer, J. Gayles, N. A. Porter, S. Sugimoto, Z. Aslam, C. J. Kinane, T. R. Charlton, F. Freimuth, S. Chadov, S. Langridge, J. Sinova, C. Felser, S. Blügel, Y. Mokrousov, and C. H. Marrows, *Phys. Rev. B* **97**, 214406 (2018).
- [7] D. Xiao, M.-Ch. Chang, and Q. Niu, *Rev. Mod. Phys.* **82**, 1959 (2010).
- [8] S. Seki and M. Mochizuki, *Skymions in Magnetic Materials* (Springer International, Cham, 2016).
- [9] T. Tanigaki, K. Shibata, N. Kanazawa, X. Yu, Y. Onose, H. S. Park, D. Shindo, and Y. Tokura, *Nano Lett.* **15**, 5438 (2015).
- [10] H. Du, J. P. Degrave, F. Xue, D. Liang, W. Ning, J. Yang, M. Tian, Y. Zhang, and S. Jin, *Nano Lett.* **14**, 2026 (2014).
- [11] D. Liang, J. P. DeGrave, M. J. Stolt, Y. Tokura, and S. Jin, *Nat. Commun.* **6**, 8217 (2015).
- [12] N. Nagaosa and Y. Tokura, *Nat. Nanotechnol.* **8**, 899 (2013).
- [13] D. A. Gilbert, A. J. Grutter, P. M. Neves, G.-J. Shu, G. Zimanyi, B. B. Maranville, F.-C. Chou, K. Krycka, N. P. Butch, S. Huang, and J. A. Borchers, *Phys. Rev. Mater.* **3**, 014408 (2019).
- [14] E. Ruff, P. Lunkenheimer, A. Loidl, H. Berger, and S. Krohns, *Sci. Rep.* **5**, 15025 (2015).
- [15] X. Z. Yu, N. Kanazawa, Y. Onose, K. Kimoto, W. Z. Zhang, S. Ishiwata, Y. Matsui, and Y. Tokura, *Nat. Mater.* **10**, 106 (2011).
- [16] X. S. Wang, H. Y. Yuan, and X. R. Wang, *Commun. Phys.* **1**, 31 (2018).
- [17] P. Bak and M. H. Jensen, *J. Phys. C Solid State Phys.* **13**, L881 (1980).
- [18] A. Bauer and C. Pfleiderer, *Phys. Rev. B* **85**, 214418 (2012).
- [19] M. N. Wilson, E. A. Karhu, A. S. Quigley, U. K. Rößler, A. B. Butenko, A. N. Bogdanov, M. D. Robertson, and T. L. Monchesky, *Phys. Rev. B* **86**, 144420 (2012).
- [20] A. S. Ahmed, J. Rowland, B. D. Esser, S. R. Dunsiger, D. W. McComb, M. Randeria, and R. K. Kawakami, *Phys. Rev. Mater.* **2**, 041401(R) (2018).
- [21] A. Hrabec, J. Sampaio, M. Belmeguenai, I. Gross, R. Weil, S. M. Chérif, A. Stashkevich, V. Jacques, A. Thiaville, and S. Rohart, *Nat. Commun.* **8**, 15765 (2017).
- [22] A. K. Nayak, V. Kumar, T. Ma, P. Werner, E. Pippel, R. Sahoo, F. Damay, U. K. Rößler, C. Felser, and S. S. P. Parkin, *Nature (London)* **548**, 561 (2017).
- [23] W. Wang, Y. Zhang, G. Xu, L. Peng, B. Ding, Y. Wang, Z. Hou, X. Zhang, X. Li, E. Liu, S. Wang, J. Cai, F. Wang, J. Li, F. Hu, G. Wu, B. Shen, and X. X. Zhang, *Adv. Mater.* **28**, 6887 (2016).
- [24] M. V. Berry, *Proc. R. Soc. London, Ser. A* **392**, 45 (1984).
- [25] L. D. Barron, in *Chirality at the Nanoscale*, edited by D. B. Amabilino (Wiley, New York, 2009), p. 1–27.
- [26] A. Neubauer, C. Pfleiderer, B. Binz, A. Rosch, R. Ritz, P. G. Niklowitz, and P. Böni, *Phys. Rev. Lett.* **102**, 186602 (2009).
- [27] W. Zhang, B. Balasubramanian, A. Ullah, R. Pahari, X. Li, L. Yue, S. R. Valloppilly, A. Sokolov, R. Skomski, and D. J. Sellmyer, *Appl. Phys. Lett.* **115**, 172404 (2019).
- [28] B. Balasubramanian, P. Manchanda, R. Pahari, Z. Chen, W. Zhang, S. R. Valloppilly, X. Z. Li, A. Sarella, L. Yue, A. Ullah, P. Dev, D. A. Muller, R. Skomski, G. C. Hadjipanayis, and D. J. Sellmyer, *Phys. Rev. Lett.* **124**, 057201 (2020).
- [29] B. Balasubramanian, P. Manchanda, R. Skomski, P. Mukherjee, B. Das, T. A. George, G. C. Hadjipanayis, and D. J. Sellmyer, *Appl. Phys. Lett.* **106**, 242401 (2015).
- [30] B. Balasubramanian, P. Manchanda, R. Skomski, P. Mukherjee, S. R. Valloppilly, B. Das, G. C. Hadjipanayis, and D. J. Sellmyer, *Appl. Phys. Lett.* **108**, 152406 (2016).
- [31] G. Kresse and D. Joubert, *Phys. Rev. B* **59**, 1758 (1999).
- [32] J. P. Perdew and A. Zunger, *Phys. Rev. B* **23**, 5048 (1981).
- [33] A. Vansteenkiste, J. Leliaert, M. Dvornik, M. Helsen, F. Garcia-Sanchez, and B. V. Waeyenberge, *AIP Adv.* **4**, 107133 (2014).
- [34] See Supplemental Material at <http://link.aps.org/supplemental/10.1103/PhysRevMaterials.5.124418> for additional details on methods and additional results.
- [35] International Centre for Diffraction Data, Powder Diffraction File Card No 04-003-6997.
- [36] International Centre for Diffraction Data, Powder Diffraction File Card No 00-006-0675.
- [37] B. D. Cullity and S. R. Stock, *Elements of X-Ray Diffraction*, 3rd ed. (Prentice Hall, Inc., Englewood Cliffs, NJ, 2001), pp. 167–171.
- [38] S. M. Stishov, A. E. Petrova, V. A. Sidorov, and D. Menzel, *Phys. Rev. B* **86**, 064433 (2012).
- [39] B. T. Thole, P. Carra, F. Sette, and G. van der Laan, *Phys. Rev. Lett.* **68**, 1943 (1992).
- [40] P. Carra, B. T. Thole, M. Altarelli, and X. Wang, *Phys. Rev. Lett.* **70**, 694 (1993).
- [41] M. Onoda and N. Nagaosa, *J. Phys. Soc. Jap.* **71**, 19 (2002).
- [42] S. X. Huang and C. L. Chien, *Phys. Rev. Lett.* **108**, 267201 (2012).
- [43] J. C. Gallagher, K. Y. Meng, J. T. Brangham, H. L. Wang, B. D. Esser, D. W. McComb, and F. Y. Yang, *Phys. Rev. Lett.* **118**, 027201 (2017).
- [44] A. Ullah, B. Balamurugan, W. Zhang, S. Valloppilly, X.-Z. Li, R. Pahari, L.-P. Yue, A. Sokolov, D. J. Sellmyer, and R. Skomski, *IEEE Trans. Magn.* **55**, 7100305 (2019).
- [45] F. N. Rybakov, A. B. Borisov, S. Blügel, and N. S. Kiselev, *Phys. Rev. Lett.* **115**, 117201 (2015).
- [46] N. Kanazawa, Y. Onose, T. Arima, D. Okuyama, K. Ohoyama, S. Wakimoto, K. Kakurai, S. Ishiwata, and Y. Tokura, *Phys. Rev. Lett.* **106**, 156603 (2011).
- [47] W. Wang, M. W. Daniels, Z. Liao, Y. Zhao, J. Wang, G. Koster, G. Rijinders, C.-Z. Chang, D. Xiao, and W. Wu, *Nat. Mater.* **18**, 1054 (2019).
- [48] Y. Fujishiro, N. Kanazawa, T. Nakajima, X. Z. Yu, K. Ohishi, Y. Kawamura, K. Kakurai, T. Arima, H. Mitamura, A. Miyake, K. Akiba, M. Tokunaga, A. Matsuo, K. Kindo, T. Koretsune, R. Arita, and Y. Tokura, *Nat. Commun.* **10**, 1059 (2019).
- [49] H. Ishizuka and N. Nagaosa, *Sci. Adv.* **4**, eaap9962 (2018).
- [50] G. Kimbell, P. M. Sass, B. Woltjes, E. K. Ko, T. W. Noh, W. Wu, and J. W. A. Robinson, *Phys. Rev. Mat.* **4**, 054414 (2020).
- [51] L. Wu, F. Wen, Y. Fu, J. H. Wilson, X. Liu, Y. Zhang, D. M. Vasiukov, M. S. Kareev, J. H. Pixley, and J. Chakhalian, *Phys. Rev. B* **102**, 220406(R) (2020).

- [52] B. Balasubramanian, T. A. George, P. Manchanda, R. Pahari, A. Ullah, R. Skomski, and D. J. Sellmyer, *Phys. Rev. Mater.* **5**, 024402 (2021).
- [53] B. Balasubramanian, K. L. Kraemer, N. A. Reding, R. Skomski, S. Ducharme, and D. J. Sellmyer, *ACS Nano* **4**, 1893 (2010).
- [54] B. Balasubramanian, B. Das, R. Skomski, W. Zhang, and D. J. Sellmyer, *Adv. Mater.* **25**, 6090 (2013).
- [55] B. Balasubramanian, P. Mukherjee, R. Skomski, P. Manchanda, B. Das, and D. J. Sellmyer, *Sci. Rep.* **4**, 6265 (2014).
- [56] M. C. Biesinger, B. P. Payne, A. P. Grosvenor, L. W. M. Lau, A. R. Gerson, and R. S. C. Smart, *Appl. Surf. Sci.* **257**, 2717 (2011).
- [57] A. P. Grosvenor, S. D. Wik, R. G. Cavell, and A. Mar, *Inorg. Chem.* **44**, 8988 (2005).
- [58] L. Schnatmann, K. Geishendorf, M. Lammel, C. Damm, S. Novikov, A. Thomas, A. Burkov, H. Reith, K. Nielsch, and G. Schierning, *Adv. Electron. Mater.* **6**, 1900857 (2020).
- [59] A. Franco and F. C. e Silva, *Appl. Phys. Lett.* **96**, 172505 (2010).
- [60] H. Kronmüller and M. Fähnle, *Micromagnetism and the Microstructure of Ferromagnetic Solids* (Cambridge University Press, Cambridge, England, 2003).
- [61] R. Skomski, *Simple Models of Magnetism* (Oxford University Press, Oxford, England, 2008).
- [62] R. Skomski and J. M. D. Coey, *Permanent Magnetism* (CRC Press, Boca Raton, FL, 1999).
- [63] E. Turgut, A. Park, K. Nguyen, A. Moehle, D. A. Muller, and G. D. Fuchs, *Phys. Rev. B* **95**, 134416 (2017).